metals

MDPI

Article

Effect of Hydrogen on the Deformation Behavior and Localization of Plastic Deformation of the Ultrafine-Grained Zr–1Nb Alloy

Ekaterina Stepanova [1,*], Galina Grabovetskaya [2], Maxim Syrtanov [1,*] and Ivan Mishin [2]

[1] School of Nuclear Science & Engineering, National Research Tomsk Polytechnic University, 30 Lenin Avenue, 634050 Tomsk, Russia

[2] Federal State Institution of Science, Institute of Strength Physics and Materials Science of the Siberian Branch of the Russian Academy of Sciences, 634055 Tomsk, Russia; grabg@ispms.tsc.ru (G.G.); mishinv1@yandex.ru (I.M.)

* Correspondence: enstepanova@tpu.ru (E.S.); maxim-syrtanov@mail.ru (M.S.); Tel.: +7-905-089-0301 (E.S.)

Received: 31 March 2020; Accepted: 28 April 2020; Published: 30 April 2020

Abstract: In this paper, comparison studies of the hydrogen effect on the structural and phase state, deformation behavior, and mechanical properties of the fine- (average grain size 4 μm) and ultrafine-grained (average element size 0.3 and 0.4 μm) Zr–1wt.%Nb (hereinafter Zr–1Nb) alloy under tension at temperatures in the range of 293–873 K were conducted. The formation of an ultrafine-grained structure is established to increase the strength characteristics of the Zr–1Nb alloy by a factor of 1.5–2 with a simultaneous reduction of its resistance to the localization of plastic deformation at the macro level and the value of deformation to failure. The presence of hydrogen in the Zr–1Nb alloy in the form of a solid solution and hydride precipitates increases its resistance to the localization of plastic deformation at the macro level if the alloy has an ultrafine-grained structure and decreases if the structure of the alloy is fine-grained. In the studied temperature range, the Zr–1Nb alloy in the ultrafine-grained state has a higher resistance to hydrogen embrittlement than the alloy in the fine-grained state.

Keywords: zirconium alloy; hydrogen; ultrafine-grained state; plastic deformation localization; hydrogen embrittlement

1. Introduction

Zirconium alloys are structural materials for core elements of nuclear power reactors due to their low neutron capture cross-section, high melting temperature, high and stable corrosion resistance in water, steam and other aggressive media, good plasticity, and high strength characteristics [1–3]. However, the strength characteristics of these alloys are insufficient for operation upon exposure to radiation. Studies performed in recent years in Russia and abroad have shown that the characteristics of metallic materials, including zirconium and its alloys, can be significantly improved in different ways, such as surface modification [4–6] or the formation of an ultrafine-grained (UFG) state [7,8]. Nowadays, all of the most widespread methods of UFG structure formation in metallic materials are based on severe plastic deformation (SPD) [9–11]. The use of SPD methods enables the sizes of structural elements in the material to be decreased to nanodimensional ones and, as a consequence, the strength characteristics to be increased by a factor of 1.5–2 [12–18].

At the same time, the rate of hydrogen absorption by metallic materials is known to be increased when the grain sizes decrease [19–22]. This fact is particularly critical for zirconium products of water-cooled nuclear power reactor cores, actively undergoing hydrogenation during operation [23,24].

Hydrogen negatively affects the plasticity of zirconium and its alloys [25]. At room temperature, this is primarily caused by the hydride formation resulting from the low solubility of hydrogen in zirconium alloys [26,27]. At elevated temperatures, hydrides can be partially or completely dissolved in zirconium and its alloys [28,29]. However, hydrogen, possessing a high diffusion mobility in metals, can be redistributed in the metal bulk under the influence of elastic stress fields, forming clusters, pores, and even hydrides in the most stressed regions, thereby increasing the probability of the brittle fracture of metals. Taking into account the foregoing, the purpose of the present work is to investigate the hydrogen effect on the deformation behavior and fracture of the UFG zirconium alloys during tension at elevated temperatures.

2. Materials and Methods

Experiments were conducted with commercial Zr–1Nb alloy (E110 grade) with the following composition (wt.%): 1Nb + Fr < 0.05 + O < 0.09; the balance is Zr.

The UFG structure of the alloy was formed by two different methods.

The first method involved pressing with the change of the deformation axis (abc-pressing method) and a gradual decrease of the temperature in the range of 973–623 K [30]. Five cycles of pressing with a pressing rate of 10^{-3} s^{-1} were performed. Each cycle included triple pressing. Deformation after single pressing was 40–50%. The total reduction e_Σ of the alloy was calculated as $e_\Sigma = \ln(l_{i-1} / l_i)$, where l is the shrinkage length and i is the number of pressing passes. After five pressing cycles, the total reduction e_Σ was about 5.5.

The second method combined preliminary hydrogenation and hot plastic deformation by pressing. The hydrogenation of the fine-grained (FG) alloy to a concentration of 0.33% (hereinafter, hydrogen concentration is indicated in weight percentage) was carried out in gas media using a Gas Reaction Controller (Advanced Materials Corporation, Pittsburgh, PA, USA) equipment at a temperature of 773 K and a hydrogen pressure of 2 atm. After the hydrogenation, the billets of the FG Zr–1Nb–0.33 wt.% H alloy were homogenized in air at 853 K for 14 h. Then, the billet was cut into two parts, the first of which was used in further studies as the initial hydrogenated FG material (hereinafter, FG Zr–1Nb–0.33H alloy). The second part of this billet was subjected to single pressing to 80% at a temperature of 923 K. The obtained structure was fixed by quenching in water. The hydrogen concentration in the samples after each stage was measured by a RHEN 602 gas analyzer (LECO, Saint Joseph, MI, USA).

An electron microscopic investigation of thin foils was carried out using a JEM-2100 (JEOL, Akishima, Tokyo, Japan) transmission electron microscope. The specimens for electron microscopy were produced by jet electropolishing in an electrolyte mixture of 80 vol.% glacial acetic acid and 20 vol.% perchloric acid. The sizes of the structural elements were measured from the relevant micrographs by the secant method [31].

The volume fractions and the lattice parameters of the phases were determined with an accuracy of ±1% and 0.0001 nm, respectively, using XRD7000S diffractometer (Shimadzu, Kyoto, Japan) with a CuK_α radiation source. The diffraction profiles were obtained by varying 2θ from 30° to 80° with a step scan of 0.02°. The data collection time per step was 2 s. The diffraction profiles were measured at room temperature and gradual heating to 1173 K with a rate of 6 K/min [32]. PowderCell 2.4 program (BAM, Berlin, Germany) was used to identify the diffraction pattern. The value of elastic stresses was found by the standard method of X-ray structural analysis for diffraction maximum broadening at their half-height using the Cauchy approximation [33,34]. Coherent scattering regions and lattice microdeformation may contribute to the total diffraction maximum broadening (β). In this case, the β value for the Cauchy approximation is determined from the relation:

$$\beta = \beta_D + \beta_\varepsilon = \frac{\lambda}{D\cos\theta} + 4\varepsilon\mathrm{tg}\theta \quad (1)$$

where β_D and β_ε are contributions of the coherent scattering regions and lattice microdeformation, respectively, to diffraction maximum broadening, λ is the X-ray wavelength, θ is angle of the diffraction plane (hkl), D is the size of the coherent scattering regions, and ε is the lattice microdeformation.

The value of elastic stresses was judged by the magnitude of the microdistortions of the crystal lattice. In order to split the contributions from coherent-scattering regions and lattice microdistortions into the diffraction peak broadening, we used the maxima from the (101) and (103) planes. The value of elastic stresses was estimated from the value of the crystal lattice microdistortions (ε).

The presence of elastic stresses was estimated from the value of the crystal lattice microdistortion (ε) determined from the equality [33,34]: $\beta_\varepsilon = 4\varepsilon \mathrm{tg}\theta$.

Tensile tests were performed at temperatures in the range of 293–973 K in the vacuum of 10^{-2} Pa with an initial strain rate of 6.9×10^{-3} s^{-1} using a PV-3012M machine (Scientific Research & Design Institute of Machines & Devices, Moscow, Russia) equipped with a tensometric system of load measurement with automatic recording of stress–strain flow curves in the load-time coordinates. For the tests at temperatures above room temperature, a thermocouple was attached to the specimen in the gauge length region. The desired temperature was controlled to ±1 K. Figure 1 shows the geometry of the test specimen.

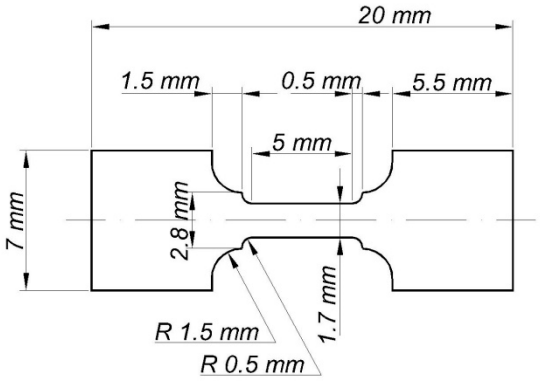

Figure 1. The geometry of the tensile-tested specimens.

Specimens were cut from billets by the electrospark method. Before testing, the specimen surfaces were subjected to mechanical grinding and chemical polishing in an electrolyte mixture containing 45 vol.% distilled water, 10 vol.% hydrofluoric acid, and 45 vol.% nitric acid. After the tensile tests, the sample surface was examined in detail with the use of a Quanta 200 3D (FEI Company, Hillsboro, OR, USA) scanning electron microscope.

3. Results

The structure of alloy in the initial FG state and state after hydrogenation is described in detail in [34–36]. It was shown that the investigated Zr–1Nb alloy had a polycrystalline structure with a grain size of 3–5 μm. Apart from the main α-Zr phase, this alloy contained a small amount (with total volume fraction not exceeding 3 vol.%) of β-Nb secondary phase (Figure 2). The secondary phase in the form of round-shaped particles was located in the grain volume and on the boundaries. The particle sizes varied from several dozen nanometers to several microns.

After hydrogenation according to the aforementioned regime, the grain size and precipitations of secondary phases in the obtained FG Zr–1Nb–0.33H alloy remain outwardly the same. However, the X-ray structure analysis revealed the presence of δ-ZrH hydride precipitates at room temperature in addition to the above-mentioned phases (Figure 2). The results of the in-situ X-ray observations of changes in the phase composition of the hydrogenated FG zirconium alloy during heating at a rate of 6 K/min showed (Figure 2) that the hydride precipitates are stable up to a temperature of 773 K. With the further rise in temperature, the δ-ZrH hydride transforms to γ-ZrH

hydride. Simultaneously with the hydride transformation in the alloy, an increase in the volume fraction of the β-Nb phase was observed.

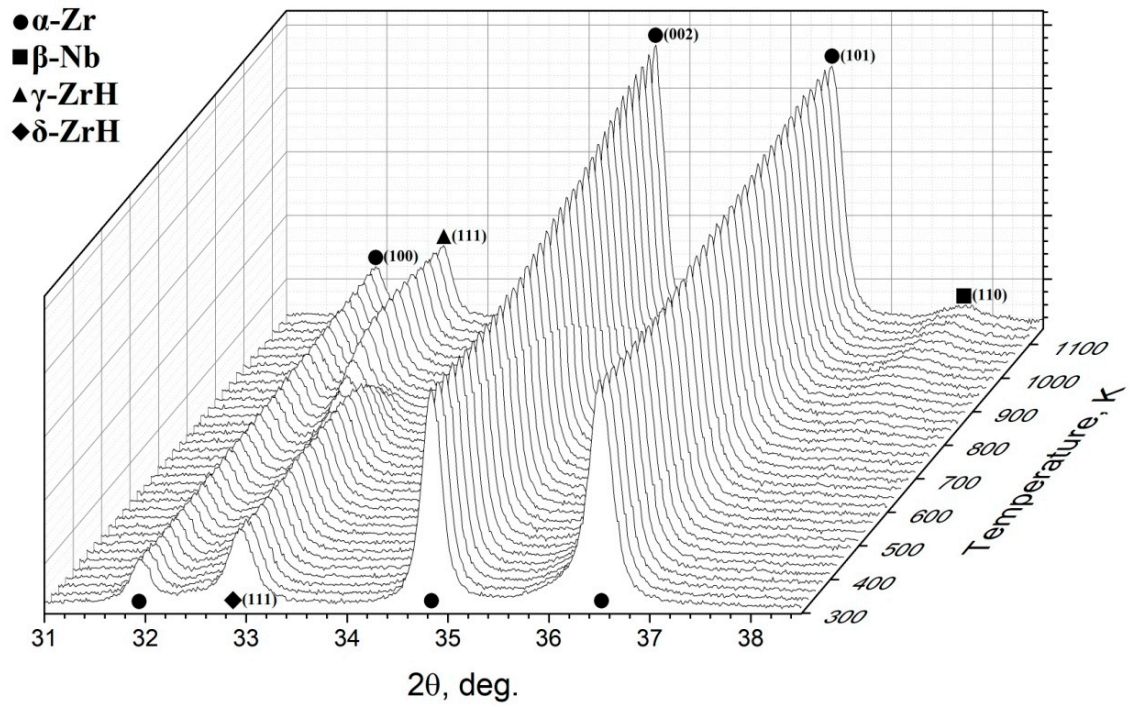

Figure 2. Parts of the diffraction pattern of the FG Zr–1Nb–0.33H alloy upon heating to 1173 K.

Figures 3 and 4 show the typical electron micrographs and the corresponding electron diffraction patterns of the UFG structure of the Zr–1Nb and Zr–1Nb–0.33H alloys. Entangled deformational contrast is clearly seen in the bright-field images of the UFG structure; thus, some structure elements are poorly distinguished. The electron diffraction patterns of the structure obtained for an area of 1.4 μm^2 show an appreciable number of reflections uniformly distributed over a circle (Figure 3a, Figure 4a). This is indicative of the presence of a large number of grain–subgrain structure elements in the unit volume and of their substantial misorientation. Some of the reflections exhibit azimuthal smearing, which is a consequence of high internal stresses. On the dark-field images of the structure, individual elements of the UFG grain–subgrain structure are visible (Figure 3b, Figure 4b). The average size of the grain–subgrain structure elements of the UFG Zr–1Nb alloy determined from the dark-field image was (0.3 ± 0.12) μm. The average size of elements of the UFG Zr–1Nb–0.33H alloy was slightly larger than the corresponding value for the Zr–1Nb alloy and was equal to (0.42 ± 0.18) μm.

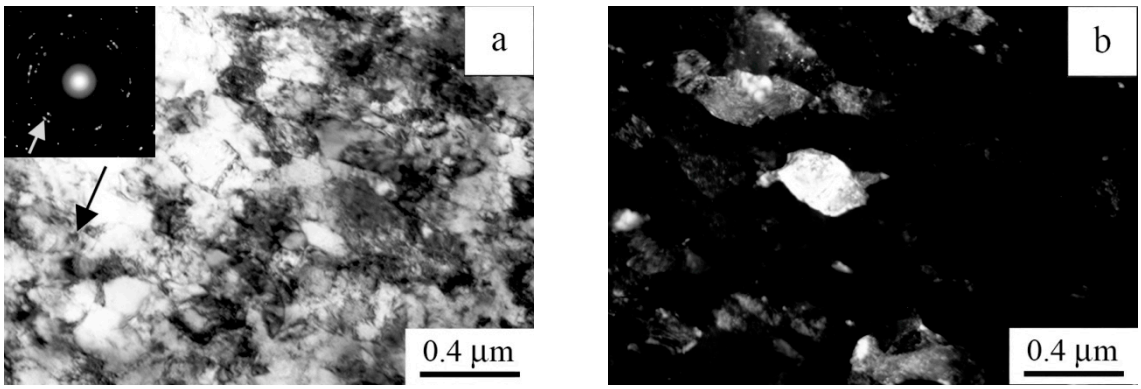

Figure 3. *Cont.*

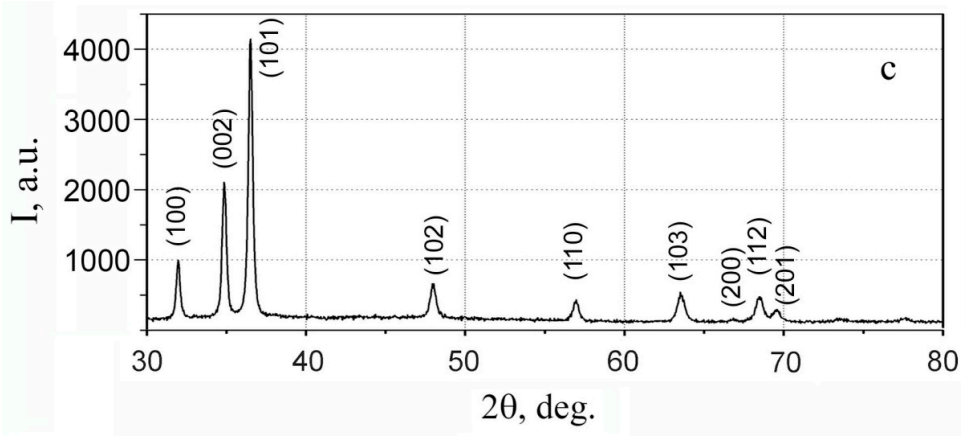

Figure 3. Microstructures [(**a**) is the bright-field image and (**b**) is the dark-field image in $(002)_{\alpha\text{-Zr}}$ reflection] and (**c**) parts of the diffraction pattern of the UFG Zr–1Nb alloy after pressing, with the change of the deformation axis and a gradual temperature decrease.

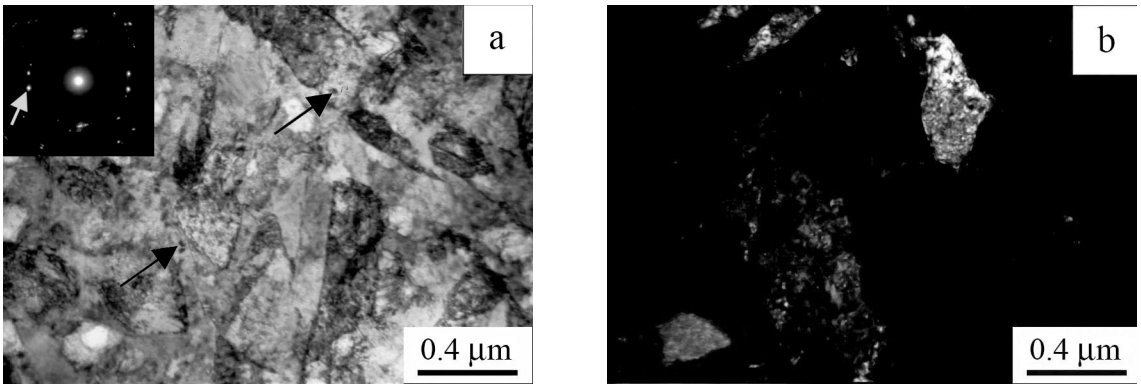

Figure 4. Microstructures of the UFG Zr–1Nb–0.33H alloy after pressing: (**a**) is the bright-field image and (**b**) is the dark-field image in $(002)_{\alpha\text{-Zr}}$ reflection.

The X-ray diffraction analysis indicated that at room temperature the UFG Zr–1Nb alloy contained only the main α-Zr (HCP) phase after pressing (Figure 3c). The UFG Zr–1Nb–0.33H alloy, conversely, had not only the main α-Zr phase after pressing but also hydride δ-ZrH precipitates (Figure 5). However, electron microscopic studies revealed that the bulk and grain boundaries of both alloys contained, in addition to the above-indicated phases, nanodimensional precipitates of the β-Nb phase (indicated by the arrows in Figure 3a, Figure 4a). In-situ observations of changes in phase composition of the studied UFG Zr–1Nb–0.33H alloy have shown that upon heating with a rate of 6 K/min the phase composition of the UFG alloy, like the FG Zr–1Nb–0.33H alloy, is qualitatively stable up to temperatures in the range of 723–773 K. With a rise in temperature above these values, we observed a δ-ZrH → γ-ZrH transformation accompanied by the simultaneous appearance of the βNb phase and gradual increase in its volume fraction (Figure 5).

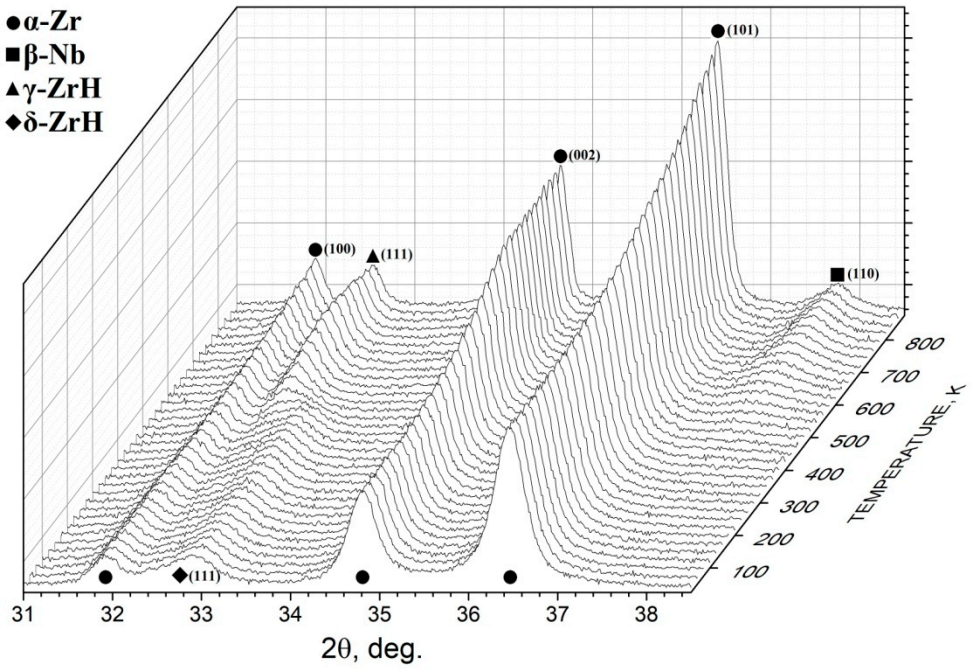

Figure 5. Parts of the diffraction pattern of the UFG Zr–1Nb–0.33H alloy upon heating to 1173 K.

Hour annealing at a temperature in the range of 573–873 K was carried out to determine the temperature interval of structural element stability for both UFG alloys. Figure 6 shows the dependence of the average size of grain–subgrain structure elements of the α-Zr phase on the annealing temperature for the UFG Zr–1Nb alloy (curve 1) and for the UFG Zr–1Nb–0.33H alloy (curve 2). It can be seen that the initial UFG structure of both alloys is stable in the temperature range of 293–723 K. However, it was found by X-ray diffraction analysis that during hour annealing in this temperature range a decrease in the internal stresses is observed. This is evidenced by a decrease in the value of internal stresses from $(2–4)\cdot10^{-3}$ to $(4–2)\cdot10^{-4}$. It should be noted that the microdeformation of the crystal lattice of the α-Zr phase in the initial Zr–1Nb alloy did not exceed 10^{-4}. An active increase in the sizes of the elements of the grain–subgrain structure of both indicated UFG alloys is observed after annealing for an hour at a temperature of 773 K. In this case, the UFG state is preserved in both alloys. With an increase of the annealing temperature to 823 K, the average size of the grain–subgrain structure elements of both UFG alloys becomes more than 1 μm.

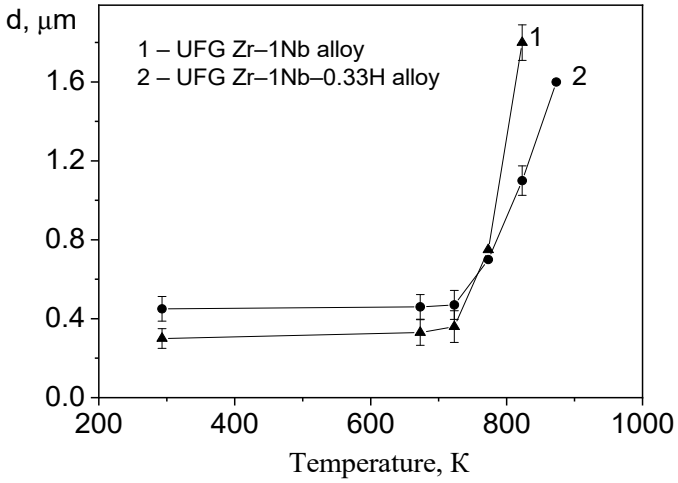

Figure 6. Temperature dependence of the change in the average grain size of the UFG structure of the zirconium alloys.

The typical tension curves for the UFG Zr–1Nb and Zr–1Nb–0.33H alloys (referred to as stress–strain curves below) at 293 and 873 K are shown in Figure 7 in the stress–strain coordinates. Generally, three deformation stages can be observed on the indicated curves: strain hardening (uniform deformation), steady-state deformation, and declining stress. The duration of these deformation stages depended on the alloy structural state, presence of hydrogen in the alloy, and test temperature.

At room temperature, more extended deformation stages are characteristic for the stress–strain curve of the FG Zr–1Nb alloy (Figure 7, curve 1). The value of the uniform deformation of the FG Zr–1Nb alloy is ~17% with a total deformation to failure of ~34%. Hydrogenation of the FG Zr–1Nb alloy to a concentration of 0.33 wt.% leads to a significant decrease in the duration of all deformation stages (Figure 7, curve 2). For example, the value of the uniform deformation of the FG Zr–1Nb alloy decreases from ~17% to ~5%. At the same time, the hydrogenation of the FG alloy leads to a significant increase in its strength characteristics.

The duration of all deformation stages of the Zr–1Nb alloy at room temperature also decreases with the formation of the UFG structure (Figure 7, curve 3). On the stress–strain curve of the UFG Zr–1Nb alloy, at room temperature, the short strain hardening stage is replaced by a sustained stage of declining stress, in which two regions with different rates of strain reduction can be distinguished. The value of the uniform deformation of the UFG Zr–1Nb alloy does not exceed 2%, which is eight times less compared to the FG alloy. The presence of hydrogen does not change the appearance of the stress–strain curve of the UFG alloy at room temperature, but slightly increases the duration of the strain hardening stage. In this case, the value of the uniform deformation increases almost twice (up to 3.8%) (Figure 7a, curve 4). An increase in the duration of all deformation stages of the Zr–1Nb and Zr–1Nb–0.33H alloys both in the FG and UFG states is observed with a rising test temperature (Figure 7b). In this case, the duration of the strain hardening stage for the Zr–1Nb–0.33H alloy in the UFG state at temperatures of 773 and 873 K becomes 1.5–2 times longer compared with the corresponding values for the FG state (Figure 7b).

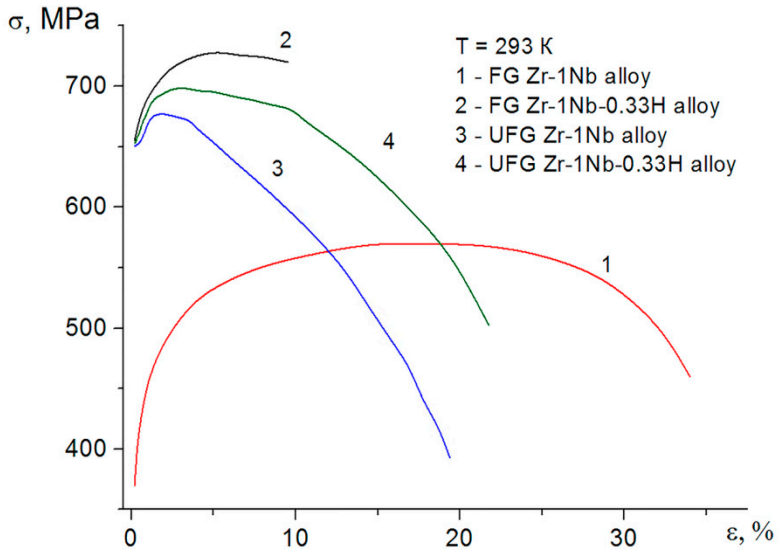

(**a**)

Figure 7. *Cont.*

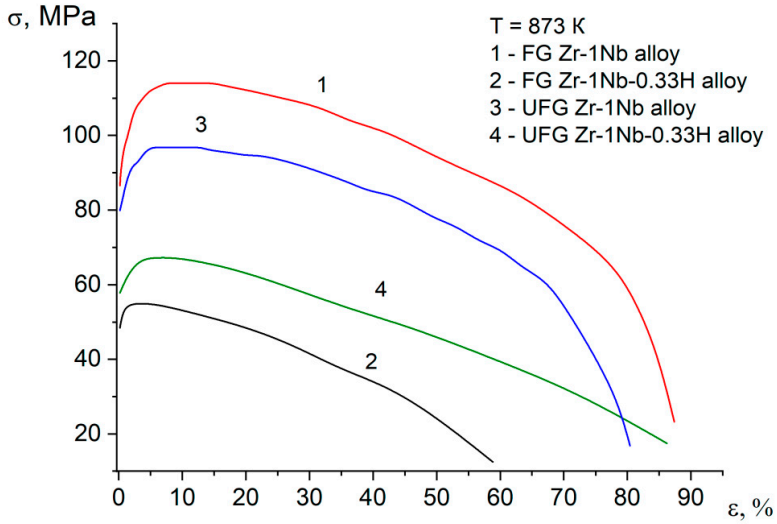

(**b**)

Figure 7. Stress–strain curves at (**a**) 293 K and (**b**) 873 K for the FG and UFG Zr–1Nb and Zr–1Nb–0.33H alloys.

The short stage of strain hardening at room temperature indicates the tendency of the UFG Zr–1Nb and Zr–1Nb–0.33H alloys toward strain localization at the macro level under tension. Strain localization on the macro level in the UFG Zr–1Nb alloy develops in two stages. Initially, there is a clearly pronounced neck, the formation of which coincides with the beginning of the stage of the declining strain on the strain–stress curve. Then, along with the strain development, bands of localized plastic deformation 0.2–0.3 mm wide appear one after another in the neck region at an angle of ~120° to one another (the development of such localized deformation bands is considered in detail in [37]). On the stress-strain curve, the appearance of macrobands of localized plastic deformation corresponds to an increase in the rate of the strain drop at the stage of declining stress (Figure 7a, curves 3 and 4). It should be noted that the tendency of the UFG zirconium alloy toward localized plastic deformation on the macro level at room temperature decreases in the presence of hydrogen (Figure 7a), but remains higher compared to the FG state.

An increased tendency toward localized plastic deformation of Zr–1Nb and Zr–1Nb–0.33H alloys in the UFG state (Figure 8c,d) in comparison with the FG state (Figure 8a,b) is demonstrated by the appearance of a sample fractured surface after testing at room temperature. Figure 8 shows that during tension at room temperature in the UFG samples of the Zr–1Nb and Zr–1Nb–0.33H alloys, a more pronounced neck is formed compared to the FG state.

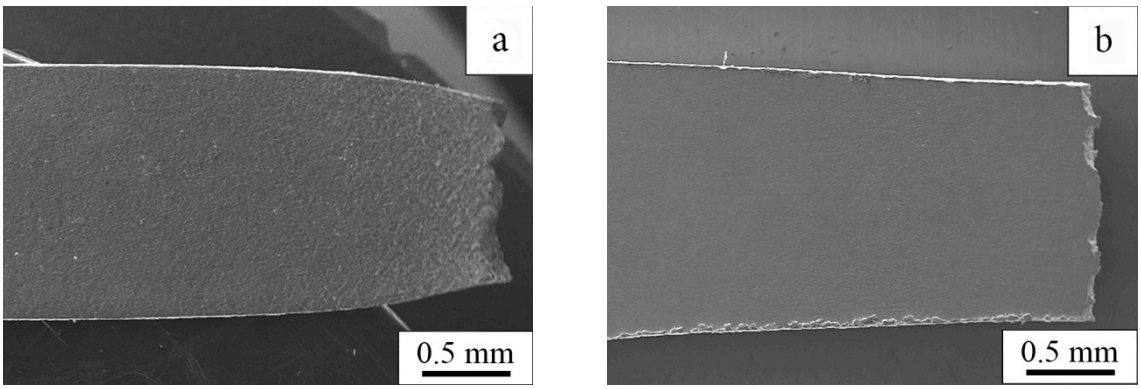

Figure 8. *Cont.*

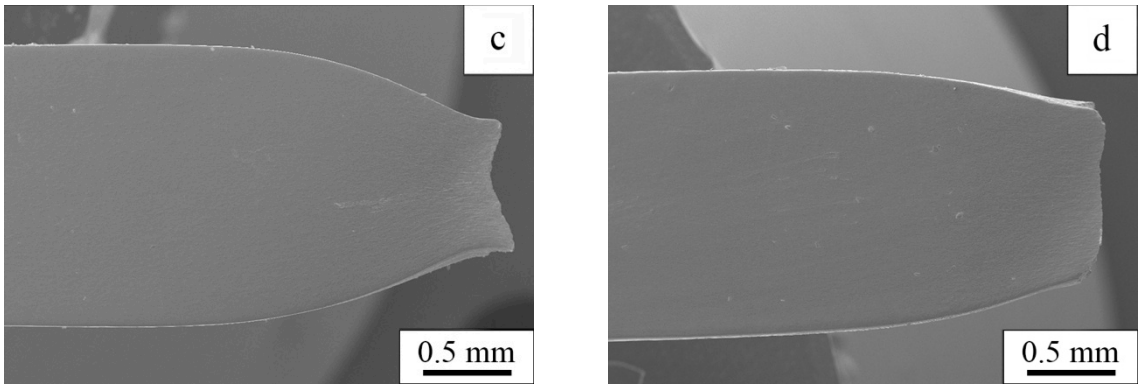

Figure 8. Fracture area of samples of the (**a**) FG Zr–1Nb, (**b**) FG Zr–1Nb–0.33H, (**c**) UFG Zr–1Nb, and (**d**) UFG Zr–1Nb–0.33H alloys after tension at temperatures of 293 K.

With an increase in the test temperature, the tendency toward localized plastic deformation of Zr–1Nb and Zr–1Nb–0.33H alloys in the UFG state decreases. At a temperature of 873 K, the localization of plastic deformation of alloys in the UFG and FG states develops almost identically. This confirms the similar appearance of the destroyed samples of Zr–1Nb and Zr–1Nb–0.33H alloys in the FG and UFG states at the indicated temperature (Figure 9). At the same time, in hydrogenated samples at elevated temperatures, the mobility of hydrogen increases. As a result, hydrogen begins to accumulate in the most stressed sections of the samples, leading to the appearance of pores and cracks, and to a decrease in the strength characteristics of the hydrogenated samples in comparison with the unhydrogenated analogues.

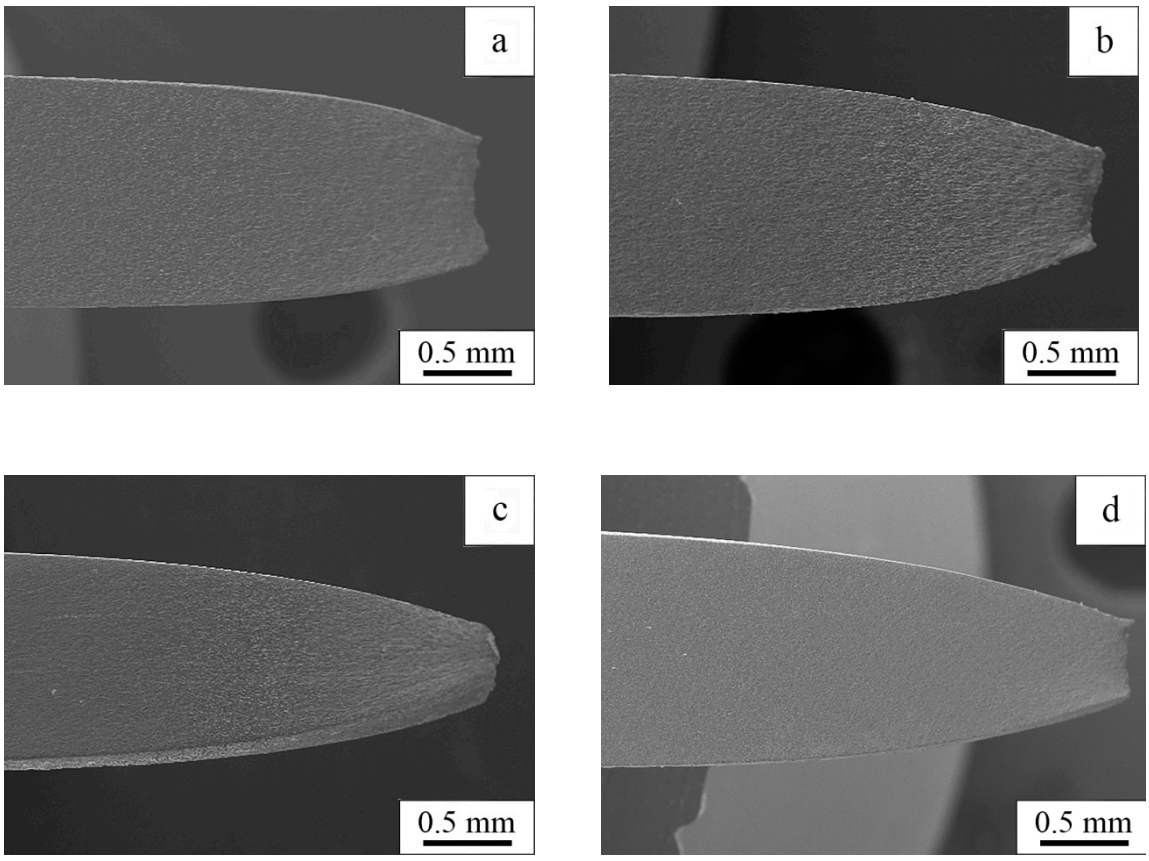

Figure 9. Fracture area of samples of the (**a**) FG Zr–1Nb, (**b**) FG Zr–1Nb–0.33H, (**c**) UFG Zr–1Nb, and (**d**) UFG Zr–1Nb–0.33H alloys after tension at 873 K.

Figure 10 shows the dependences of the values of the yield strength ($\sigma_{0.2}$) and the deformation to failure (δ) on the test temperature of Zr–1Nb and Zr–1Nb–0.33H alloys in the FG and UFG states. In Figure 10a, it can be seen that the formation of the UFG structure in the Zr–1Nb alloy leads to an increase in strength and a decrease in plastic characteristics in the temperature range of 293–773 K, at which the UFG structure is preserved. At a temperature of 873 K, the strength and plastic properties of the Zr–1Nb alloy in the FG and UFG states are close.

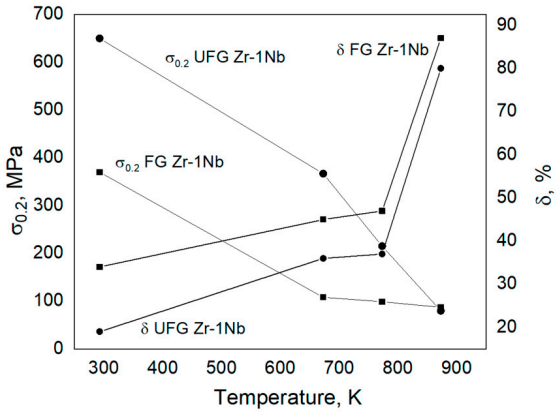

(**a**)

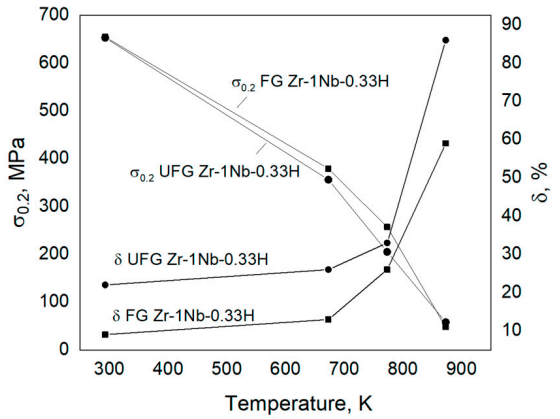

(**b**)

Figure 10. Dependences of the yield strength ($\sigma_{0.2}$) and the deformation to failure (δ) on the test temperature for the (**a**) Zr–1Nb and (**b**) Zr–1Nb–0.33H alloys in the FG and UFG states.

However, the most interesting results were obtained during the formation of the UFG structure in the Zr–1Nb–0.33H alloy. Figure 10b shows that the UFG structure formation in the Zr–1Nb–0.33H alloy leads to an increase in the value of the deformation to failure compared to the FG hydrogenated alloy in the entire temperature range studied. At the same time, the $\sigma_{0.2}$ values of the UFG Zr–1Nb–0.33H alloy differ slightly from the corresponding values for the FG Zr–1Nb–0.33H alloy. These results indicate a higher resistance to hydrogen embrittlement of the Zr–1Nb alloy in the UFG state in comparison with the FG state.

The higher resistance to hydrogen embrittlement of the UFG Zr–1Nb–0.33H alloy in comparison with the FG state is also evidenced by the sample fracture surface after tension at room temperature (Figure 11). Cracks are observed on the fracture surface of the Zr–1Nb–0.33H alloy in the FG state

(Figure 11a). At the same time, there are no cracks on the fracture surface of the UFG Zr–1Nb–0.33H alloy, and the fracture surface has the form of a viscous dimple fracture (Figure 11b).

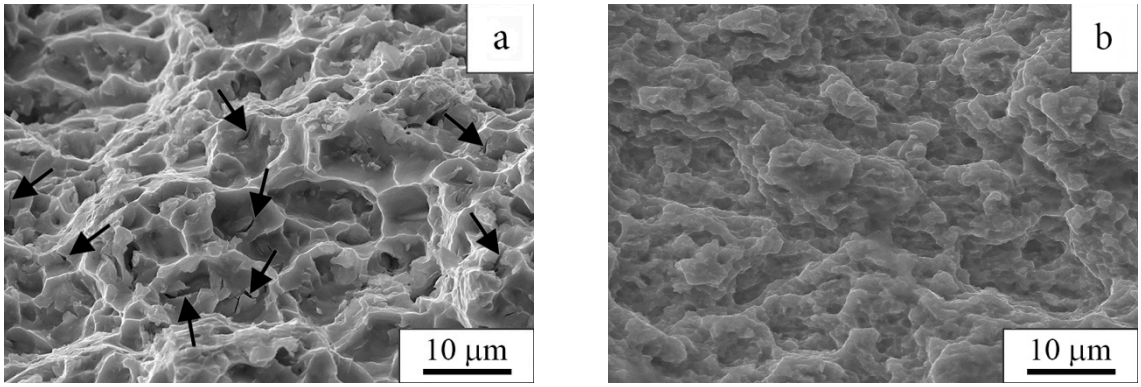

Figure 11. Fracture surface of the Zr–1Nb–0.33H alloy samples after tension at room temperature: (**a**) FG state and (**b**) UFG states.

4. Discussion

It is known [38] that an increase in the strength characteristics of metallic materials in the UFG state obtained by SPD methods is associated not only with a decrease in grain size but also with an increase in the density of defects and the presence of nonequilibrium grain boundaries that create long-range stress fields. The presence of high internal stresses impedes the movement of dislocations, which leads to the development of cooperative deformation modes: meso- and macrobands of localized deformation [39]. On the other hand, there is an opinion [40] according to which the presence of hydrogen in the solid solutions of some metals (Nb, V, Ti, and Fe) and alloys on their base not only strengthens the solid solution but also relieves the nucleation of dislocations and increases their mobility. We can suppose that the weaker tendency to plastic deformation localization of the UFG Zr–1Nb–0.33H alloy at room temperature in comparison with the UFG Zr–1Nb alloy is connected with the easier nucleation of dislocations and the increase of their mobility in the presence of hydrogen.

It was noted above that in the process of hourly annealing at elevated temperatures a decrease in internal stresses occurs in UFG Zr–1Nb and UFG Zr–1Nb–0.33H alloys. Therefore, it can be assumed that during heating and subsequent tension at elevated temperatures a decrease in internal stresses also occurs in UFG Zr–1Nb and Zr–1Nb–0.33H alloys. This will contribute to a more active movement of dislocations, with an increase in the test temperature and, as a result, an observed decrease in the tendency of these UFG alloys toward localized plastic deformation and rise in the value of uniform deformation.

The substantially smaller effect of hydrogen on the strength and plastic characteristics of the Zr–1Nb–0.33H alloy in the UFG state as compared to the FG state is apparently associated with the small sizes of the UFG structure elements. This assumption is based on the Petch–Straw law, according to which the dependence of the breaking point (σ_{br}) on the grain size for alloys containing hydride precipitates in the form of plates is described by the following equation [38]:

$$\sigma_{br} = \sigma_0 + k_{br} \cdot d^{-1/2}, \quad (2)$$

where $k_{br} = [6\gamma G/(1-\mu)]^{-1/2}$; G–shear modulus; γ–surface energy; μ–Poisson's ratio; and d–grain size.

From Equation (2), it follows that with a decreasing grain size, the value of σ_{br} increases with the indicated form of hydride precipitates. If hydride particles are located along grain boundaries, then, as shown in [41], for the same grain the size and hydride amount, σ_{br} initially increases with a growth in the relative fraction (approximately 0.2–0.3) of the length of the boundaries containing hydrides, and then decreases. Hence, with a decrease in the grain size and the same size of hydride precipitates, the maximum value of σ_{br} is achieved with a larger length of boundaries containing hydrides, i.e.,

with more hydrides. Consequently, the transition of UFG alloys to brittle fracture can occur with large values of σ_{br} compared to FG alloys, both in the case of plate hydride precipitates in the grain bulk and in the case of their precipitation in the form of particles at grain boundaries.

5. Conclusions

This work is devoted to the investigation of the hydrogen effect on the deformation behavior and fracture of UFG zirconium alloys during tension at elevated temperatures. The main conclusions are the following:

(1) The formation of an ultrafine-grained structure in the Zr–1Nb alloy by methods of severe plastic deformation leads to a significant (by 1.5–2 times) increase in its values of tensile strength and yield strength, while raising the tendency to localize plastic deformation and reducing the deformation to failure.

(2) The hydrogenation of the fine-grained Zr–1Nb alloy to a concentration of 0.33 wt.% increases its tensile and yield strengths by a factor of 1.5–2.5, while the deformation to failure decreases by a factor of 2–3.5. The presence of hydrogen in the ultrafine-gained Zr–1Nb alloy up to a concentration of 0.33 wt.% practically does not affect its strength and plastic characteristics.

(3) The formation of an ultrafine-grained state in the Zr–1Nb alloy using methods of severe plastic deformation increases its resistance to hydrogen embrittlement.

(4) In the studied temperature range, the resistance to hydrogen embrittlement of the Zr–1Nb alloy in the UFG state is higher than in the FG state.

Author Contributions: E.S. carried out hydrogenation and mechanical testing. G.G. performed mechanical testing. I.M. performed TEM measurements. M.S. conducted XRD measurements and prepared the manuscript according to the guidelines. All authors have read and agreed to the published version of the manuscript.

Funding: This research was funded by the Russian Foundation for Basic Research, research project No. 18-08-00158.

Acknowledgments: This work was carried out within the framework of the Competitiveness Enhancement Program of National Research Tomsk Polytechnic University.

Conflicts of Interest: The authors declare no conflict of interest.

References

1. Keys, L.H.; Johanson, G.; Malin, A.S. The physical metallurgy of high strength zirconium alloys. *J. Nucl. Mater.* **1976**, *59*, 137–148. [CrossRef]
2. Motta, A.T.; Yilmazbayhan, A.; Da Silva, M.J.G.; Comstock, R.J.; Was, G.S.; Busby, J.T.; Gartner, E.; Peng, Q.; Jeong, Y.H.; Park, J.Y. Zirconium alloys for supercritical water reactor applications: Challenges and possibilities. *J. Nucl. Mater.* **2007**, *371*, 61–75. [CrossRef]
3. Zinkle, S.J.; Was, G.S. Materials challenges in nuclear energy. *Acta Mater.* **2013**, *61*, 735–758. [CrossRef]
4. Ryabchikov, A.I.; Kashkarov, E.B.; Shevelev, A.E.; Obrosov, A.; Sivin, D.O. Surface modification of Al by high-intensity low-energy Ti-ion implantation: Microstructure, mechanical and tribological properties. *Surf. Coat. Technol.* **2019**, *372*, 1–8. [CrossRef]
5. Pushilina, N.S.; Lider, A.M.; Kudiyarov, V.N.; Chernov, I.P.; Ivanova, S.V. Hydrogen effect on zirconium alloy surface treated by pulsed electron beam. *J. Nucl. Mater.* **2015**, *456*, 311–315. [CrossRef]
6. Hao, S.; Dong, C.; Li, M.; Zhang, X.; Wu, P. Surface modification of metallic materials by high current pulsed electron beam. *Int. J. Mod. Phys. B* **2009**, *23*, 1713–1718. [CrossRef]
7. Koch, C.C.; Langdon, T.G.; Lavernia, E.J. Bulk Nanostructured Materials. *Metall. Mat. Trans. A* **2017**, *48*, 5181–5199. [CrossRef]
8. Valiev, R.Z.; Alexandrov, I.V. *Nanostructured Materials Produced by Severe Plastic Deformation*; Logos: Moscow, Russia, 2000.
9. Rudskoy, A.I.; Bogatov, A.A.; Nukhov, D.S.; Tolkushkin, A.O. New Method of Severe Plastic Deformation of Metals. *Met. Sci. Heat Treat.* **2018**, *60*, 3–6. [CrossRef]
10. Zhilyaev, A.P.; Langdon, T.G. Using high-pressure torsion for metal processing: Fundamentals and applications. *Prog. Mater. Sci.* **2008**, *53*, 893–979. [CrossRef]

11. Valiev, R.Z.; Zhilyaev, A.P.; Langdon, T.G. *Bulk Nanostructured Materials: Fundamentals and Applications*; John Wiley & Sons, Inc.: Hoboken, NJ, USA, 2014. [CrossRef]
12. Valiev, R.Z.; Estrin, Y.; Horita, Z.; Langdon, T.G.; Zehetbauer, M.J.; Zhu, Y.T. Fundamentals of superior properties in bulk NanoSPD materials. *Mater. Res. Lett.* **2016**, *4*, 1–21.
13. Nikulin, S.A.; Rozhnov, A.B.; Rogachev, S.O.; Turchenko, V.A. Investigation of structure, phase composition, and mechanical properties of Zr–2.5% Nb alloy after ECAP. *Mater. Res.* **2016**, *169*, 223–226. [CrossRef]
14. Yang, Z.N.; Xiao, Y.Y.; Zhang, F.C.; Yan, Z.G. Effect of cold rolling on microstructure and mechanical properties of pure Zr. *Mater. Sci. Eng. A* **2012**, *556*, 728–733. [CrossRef]
15. Valiev, R.Z.; Estrin, Y.; Horita, Z.; Langdon, T.G.; Zehetbauer, M.J.; Zhu, Y.T. Producing bulk ultrafine-grained materials by severe plastic deformation: Ten years later. *JOM* **2016**, *68*, 1216–1226. [CrossRef]
16. Yuan, C.; Fu, R.; Zhang, F.; Zhang, X.; Liu, F. Microstructure evolution and mechanical properties of nanocrystalline zirconium processed by surface circulation rolling treatment. *Mater. Sci. Eng. A.* **2013**, *565*, 27–32. [CrossRef]
17. Kassner, M.E.; Perez-Prado, M.T.; Hayes, T.A.; Jiang, L.; Barrabes, S.R.; Lee, I.F. Elevated temperature deformation of Zr to large strains. *J. Mater. Sci.* **2013**, *48*, 4492–4500. [CrossRef]
18. Jiang, L.; Perez-Prado, M.T.; Gruber, P.A.; Arzt, E.; Ruano, O.A.; Kassner, M.E. Texture, microstructure and mechanical properties of equiaxed ultrafine-grained Zr fabricated by accumulative roll bonding. *Acta Mater.* **2008**, *56*, 1228–1242. [CrossRef]
19. Soyama, J.; Floriano, R.; Leiva, D.R.; Guo, Y.; Junior, A.M.J.; Da Silva, E.P.; Pinto, H.C.; Bolfarini, C.; Kiminami, C.S.; Botta, W.J. Severely deformed ZK60 + 2.5% Mm alloy for hydrogen storage produced by two different processing routes. *Int. J. Hydrogen Energy* **2016**, *41*, 11284–11292. [CrossRef]
20. Geld, P.V.; Ryabov, P.A.; Kodes, E.S. *Hydrogen and Imperfections of Metal Structure*; Metallurgiya: Moscow, Russia, 1979. (In Russian)
21. Leiva, D.R.; Jorge, A.M.; Ishikawa, T.T.; Huot, J.; Fruchart, D.; Miraglia, S.; Kiminami, C.S.; Botta, W.J. Nanoscale grain refinement and H-sorption properties of MgH_2 processed by high-pressure torsion and other mechanical routes. *Adv. Eng. Mater.* **2010**, *12*, 786–792. [CrossRef]
22. Jorge, A.M.; Prokofiev, E.; De Lima, G.F.; Rauch, E.; Veron, M.; Botta, W.J.; Kawasaki, M.; Langdon, T.G. An investigation of hydrogen storage in a magnesium-based alloy processed by equal-channel angular pressing. *Int. J. Hydrogen Energy* **2013**, *38*, 8306–8312. [CrossRef]
23. Zielinski, A.S.; Sobieszczyk, S. Hydrogen-enhanced degradation and oxide effects in zirconium alloys for nuclear applications. *Int. J. Hydrogen Energy* **2011**, *36*, 8619–8629. [CrossRef]
24. Suman, S.; Khan, M.K.; Pathak, M.; Singh, R.N.; Chakravartty, J.K. Hydrogen in Zircaloy: Mechanism and its impacts. *Int. J. Hydrogen Energy* **2015**, *40*, 5976–5994. [CrossRef]
25. Zhao, C.; Song, X.; Yang, Y.; Zhang, B. Hydrogen absorption cracking of zirconium alloy in the application of nuclear industry. *Int. J. Hydrogen Energy* **2013**, *38*, 10903–10911. [CrossRef]
26. Sawatzky, A.; Ells, C.E. *Understanding Hydrogen in Zirconium, Zirconium in the Nuclear Industry. Proceedings of the 12th International Symposium, Washington, DC, USA, 9–11 February 2020*; ASTM STP 1354; Sabol, H.G.P., Moan, G.D., Eds.; American Society for Testing and Materials: West Conshohocken, PA, USA, 2000; pp. 32–48.
27. Tewari, R.; Srivastava, D.; Dey, G.K.; Chakravarty, J.K.; Banerjee, S. Microstructural evolution in zirconium-based alloys. *J. Nucl. Mater.* **2008**, *383*, 153–171. [CrossRef]
28. Goltsov, V.A. (Ed.) *Progress in Hydrogen Treatment of Materials*; Kassiopeya: Donetsk-Coral Gables, Ukraine, 2001; p. 543.
29. Bair, J.; Zaeem, M.A.; Tonks, M. A review on hydride precipitation in zirconium alloys. *J. Nucl. Mater.* **2015**, *466*, 12–20. [CrossRef]
30. Grabovetskaya, G.P.; Mishin, I.P.; Stepanova, E.N.; Chernov, I.P.; Bulynko, D.Y. Forming and deformation behavior of the ultrafine-grained Zr–1Nb alloy. *Steel Transl.* **2015**, *45*, 111–115. [CrossRef]
31. Saltikov, S.A. *Stereometric Metallography*; Metallurgiya: Moscow, Russia, 1970. (In Russian)
32. Syrtanov, M.; Garanin, G.; Kashkarov, E.; Pushilina, N.; Kudiiarov, V.; Murashkina, T. Laboratory X-ray Diffraction Complex for In Situ Investigations of Structural Phase Evolution of Materials under Gaseous Atmosphere. *Metals* **2020**, *10*, 447. [CrossRef]
33. Gorelik, S.S.; Skakov, Y.A.; Rastorguev, L.N. *X-Ray and Electron-Optical Analysis*; Publishing House of Moscow Institute of Steels and Alloys: Moscow, Russia, 2002. (In Russian)

34. Grabovetskaya, G.P.; Stepanova, E.N.; Dubrovskaya, A.S. Effect of hydrogen on the creep of the ultrafine-grained zirconium Zr–1Nb alloy at 673 K. *Int. J. Hydrogen Energy* **2017**, *42*, 22633–22640. [CrossRef]
35. Stepanova, E.N.; Grabovetskaya, G.P.; Mishin, I.P.; Kudiiarov, V.N. Structural and phase state and deformation behavior of the hydrogenated ultrafine-grained Zr–1Nb Alloy. *AIP Conf. Proc.* **2016**, *1783*, 020219.
36. Stepanova, E.N.; Grabovetskaya, G.P.; Mishin, I.P.; Bulinko, D.Y. Structure and mechanical properties of a Zr-1Nb Alloy, obtained by the method of severe plastic deformation. *Mater. Today Proc.* **2015**, *2*, 365–369. [CrossRef]
37. Dudarev, E.F.; Bakach, G.P.; Grabovetskaya, G.P.; Kolobov, Y.R.; Kashin, O.A.; Chernova, L.V. Plastic deformation behavior and localization in submicrocrystalline titanium at meso- and macroscale levels. *Phys. Mesomech.* **2001**, *4*, 89–95.
38. Meyers, M.A.; Mishra, A.; Benson, D.J. Mechanical properties of nanocrystalline materials. *Prog. Mater. Sci.* **2006**, *51*, 427–556. [CrossRef]
39. Panin, V.E.; Egorushkin, V.E.; Panin, A.V. Physical mesomechanics of a deformed solid as a multilevel system. I. Physical fundamentals of the multilevel approach. *Phys. Mesomech.* **2006**, *9*, 9–20.
40. Robertson, I.M. The effect of hydrogen on dislocation dynamics. *Eng. Fract. Mech.* **2001**, *68*, 671–692. [CrossRef]
41. Kolachev, B.A.; Livanov, V.A.; Buhanova, A.A. *Mechanical Properties of Titanium and Its Alloys*; Metallurgiya: Moscow, Russia, 1974. (In Russian)